Modern Physics Letters B, Vol. 23, No. 8 (2009) 1101–1109

COMPUTER SIMULATION OF ZnO FIELD-EFFECT TRANSISTOR FOR HIGH-POWER AND HIGH-TEMPERATURE APPLICATIONS USING THE MONTE CARLO METHOD

H. ARABSHAHI

Department of Physics, Ferdowsi University of Mashhad,
P.O. Box 91775-1436, Mashhad, Iran,
arabshahi@um.ac.ir

Received 17 May 2008
Revised 15 October 2008

The steady-state and transient electron transport in ZnO field effect transistor have been studied using an ensemble Monte Carlo simulation which takes into account the hot-electron transport phenomena. The simulated device geometries and doping are matched to the nominal parameters described for the experimental structures as closely as possible, and the predicted I–V and transfer charateristics for the intrinsic devices show fair agreement with the available experimental data. Simulations of the effect of modulating the gate bias have also been carried out to test the device response and derived the frequency bandwidth. The value of 80 ± 5 GHz has been derived for the intrinsic current gain cut-off frequency of the ZnO MESFETs.

Keywords: Steady-state; transient; cut-off frequency; frequency bandwidth.

1. Introduction

Wide band gap semiconductors, such as 6H-SiC (3.0 eV, at 2 K) and GaN (3.5 eV), have come to the forefront in the past decade because of an increasing need for short-wavelength photonic devices and high-power, high-frequency electronic devices, and because of breakthroughs in high-quality growths of these materials. On the other hand, another wide band gap semiconductor, ZnO (3.4 eV), has not received the same attention, probably because this material has been perceived as being useful only in its polycrystalline form. Indeed, polycrystalline ZnO has found numerous applications in such diverse areas as facial powders, piezoelectric transducers, varistors, phosphors, and transparent conducting films. Recently, however, large area bulk growth has been achieved,[1] and, furthermore, several epitaxial methods have produced excellent material.[2–10] Also, quantum wells have been successfully grown, by alloying with Mg or Cd.[11] Thus, ZnO is now being proposed for the same applications as those listed above for GaN and SiC. In fact, ZnO has several fundamental advantages over its chief competitor, GaN:

(i) Its free exciton is bound with 60 meV, much higher than that of GaN (~ 24 meV).

(ii) It has a native substrate.
(iii) Wet chemical processing is possible.
(iv) It is more resistant to radiation damage (although both are much better than Si or GaAs).

The metal semiconductor field effect transistor (MESFET) is one of the most favored devices in the construction of large scale integrated circuits because of its simplicity of construction, the comparative lack of dopant diffusion problems and the resultant high packing densities. Whilst the preferred semiconductor is still silicon, the industry is now tooling up for wide band gap semiconductors like ZnO production, which offers high electron mobility and hence the prospect of greater frequency operating rates. Their direct band gap furthermore allows easier integration with optical devices. For this reason, ZnO MESFETs have received much attention to understand the basic principles of their operation. Theoretical methods like Monte Carlo simulation have been used to a great extent in this effort because they allow an essentially exact solution of the Boltzmann transport equation and are subject only to statistical errors, unlike drift diffusion models which cannot accurately treat the hot-electron effects that are present to a high degree in GaN devices.[12–14] ZnO offers the prospect of mobilities comparable to GaN and is increasingly being developed for the construction of optical switches. Other authors have also pointed out the potential importance of ZnO and a few simple devices have been simulated.[15]

In this paper, we report a Monte Carlo simulation which is used to model electron transport in wurtzite ZnO MESFET. The device geometries and transport model are described in Sec. 2, and simulation results are provided in Sec. 3.

2. The Simulation

Our ensemble Monte Carlo model incorporates complete Γ-U-K band structures. Material parameters such as non-parabolicities, valley separations, and transverse and longitudinal effective masses are obtained either from experimental results or from pseudopotential calculations (Table 1). A constant timestep discretization scheme is chosen in the Monte Carlo procedure, which allows us to track the time evolution of the electronic transport as well as to determine the position of all sample electrons at given instances of time. Consequently, the electron concentration as a function of space and time can be determined and Poisson's equation can be solved to obtain the self-consistent electric field.

In order to minimize the statistical fluctuations, always associated with the stochastic Monte Carlo method, we choose 20 000 electron paticles for the simulation and a timestep of 10 fs for the readjustment of the electric field. A charge assignment scheme is also used to suppress the fluctuations. Each particle represents a cloud of electrons. The charge of the particle is assigned to its nearest four background mesh points proportionally to the position of the particle in the cell. To make the charge assignment more efficient, field cell size used for the central region is 30 nm^2 (horizontal $\times$ vertical), but that in the high-doped source and drain implants is

Table 1. Important parameters used in our simulations for ZnO material.

	ZnO
Density ρ (kgm^{-3})	5600
Longitudinal sound velocity v_s (ms^{-1})	6400
Low-frequency dielectric constant ϵ_s	8.2
High-frequency dielectric constant ϵ_∞	3.7
Acoustic deformation potential D (eV)	15
Polar optical phonon energy $\hbar\omega_{op}$ (eV)	0.072
Piezoelectric constant h_{pz} C/m^2	0.89
Band Gap E_g (eV)	3.43
Nonparabolicity α (eV^{-1})	0.323
Electron effective mass (m_0):	
$m^*_\parallel$ (Γ-A direction)	0.27
$m^*_\perp$ (Γ-M direction)	0.4

finer (10 nm^2).

Electrons in the bulk are scattered by ionized impurities and by bulk acoustic and non-polar optical phonon modes. Intervalley scattering by the absorption and emission of long wavelength acoustic and optic phonons have also been considered in the model. As described in detail,[16,17] model devices are built up as a series of joined rectangular regions, with the electric field cell sizes matched along the join between each region. Each region can consist of multiple layers of different alloy composition and doping/compensation density. The ZnO MESFET can be described simply by three regions (Fig. 1), representing source and drain doping implants and a central region containing the supply layers.

Figure 1 shows a schematic of the modeled ZnO MESFET. The overall device length is 2.5 μm in the x-direction and the device has a 0.2 μm gate length and 0.15 μm source and drain length. The source and drain have ohmic contacts and the gate in Schottky contact in 1 eV to represent the contact potential at Au/Pt. The source and drain regions are doped to 2×10^{24} m^{-3} electron concentration and the top and down buffer layers are doped to 2×10^{23} m^{-3} and 5×10^{22} m^{-3} electron concentrations, respectively.

Subsequent to modeling the steady-state characteristics, simulations of the effect of modulating the gate bias have also been carried out, in order to test the drain current respose and drive the cut-off frequency corresponding to unit current gain. The frequency response was investigated by applying truncated sinc voltage pulse to both gate contacts of the ZnO MESFET. The time-dependence of the voltage signal is

$$V_{\text{gate}}(t) = V_0 + V_{\text{amplitude}} \times \frac{\sin\omega(t-T/2)}{\omega(t-T/2)} \tag{1}$$

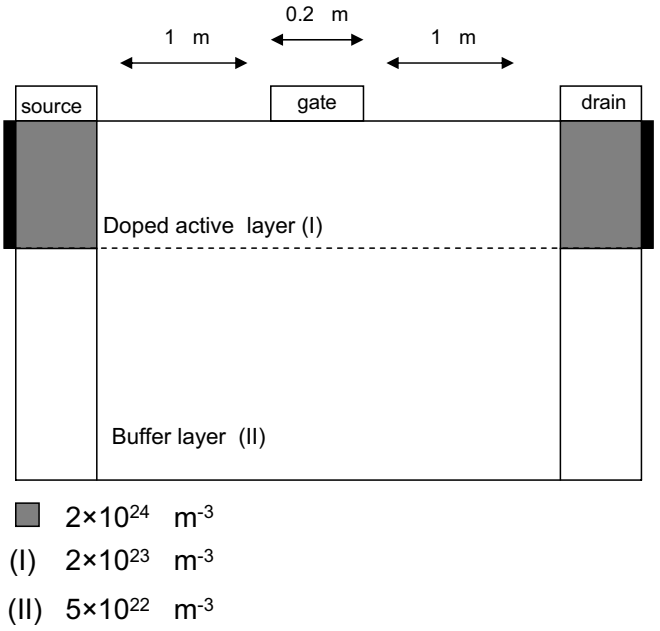

Fig. 1. The two-dimensional model of ZnO MESFET. The modeled structure is divided into three regions, as indicated. Electron particles are initially distributed keeping all regions charge neutral. The location of the source and the drain implants and the top and back buffer layer are marked.

with $\omega = 2\pi T/T_{\text{mini}}$, where V_0 is the steady gate bias upon which the modulation signal is superimposed, $V_{\text{amplitude}}$ is the peak voltage during the signal, T is the duration of the signal, and T_{mini} is the duration of each mini-cycle within that signal. In this instance ten mini-cycles have been used. A 100 ps duration sinc-form pulse containing ten mini-cycles (upper diagram, Fig. 6) has the specific advantage of providing a flat frequency spectrum up to 100 GHz, with 10 GHz resolution.

3. Results

Figure 2 shows the simulated drain current–voltage characteristic for the ZnO MESFET, with the gate voltage descending from -1 V to -13 V in -2 intervals. The simulated characteristics at room temperature show good saturation behavior with a knee voltage around 20–30 V and a saturation drain current of about 900 mAmm^{-1} for $V_{gs} = -1$ V. The high drain current density is encouraging for the use of ZnO for high power applications. It is also clear that the device is not completely pinched-off even at large negative gate bias ($V_{gs} = -13$ V) which is due to strong electron injection into the buffer layer at high electric fields. An increasing fraction of the drain current flows through the buffer as the drain voltage increases.

The spatial distribution of hot electrons throughout the device for each valley at $V_{gs} = -1$ V and $V_{ds} = 20$ V for room temperature operation is shown in Fig. 3.

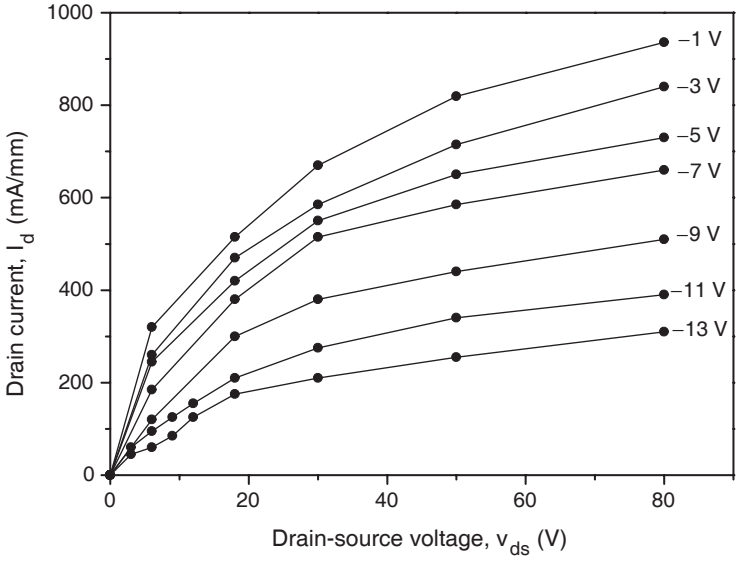

Fig. 2. Simulated current–voltage characteristic for the ZnO MESFET at 300 K. The gate voltage ranges from −1 to −13 V, in −2 V intervals. Note the knee voltage at around 20–30 V.

Electrons are seen to exist in the upper valleys only to the right of the high field region, which exists on the drain side of the gate, because it is only there that the electrons have attained enough energy to be scattered into the satellite conduction valleys. Also note there is an injection of electrons from the channel into the buffer layer, a process which is eventually opposed by the electric field created by the resulting negative space charge in the buffer layer. Figure 3 also shows that the distribution of electrons occupying the upper valleys extends a significant way towards the drain region where the electric field is much lower. This is a result of the finite time that it takes for phonon-scattering to return the electrons to the Γ-valley.

Figures 4 and 5, respectively, show the steady state Γ-valley band profile and the total electron density as a function of distance from the source when the drain-source potential drop is 20 V and the gate voltage is −1 V. Note that almost all the drain-source potential is dropped within the gate-drain region of the channel, leaving a flat potential profile near the source and drain. As electrons move towards the drain, they lose potential energy and gain sufficient kinetic energy to transfer to the upper conduction valleys where their drift velocity is reduced. Figure 5 demonstrates the electron density through the device. The gate depletion region is clearly seen where the electron density is several orders of magnitude lower than it is near the source and drain.

Figure 6 shows the sinc voltage signal applied to the gate (top diagram), the drain current response (middle diagram) and the gate current (lower diagram), for the simulated ZnO MESFET. In Fig. 6, the gate current (I_{gate}) is the electric

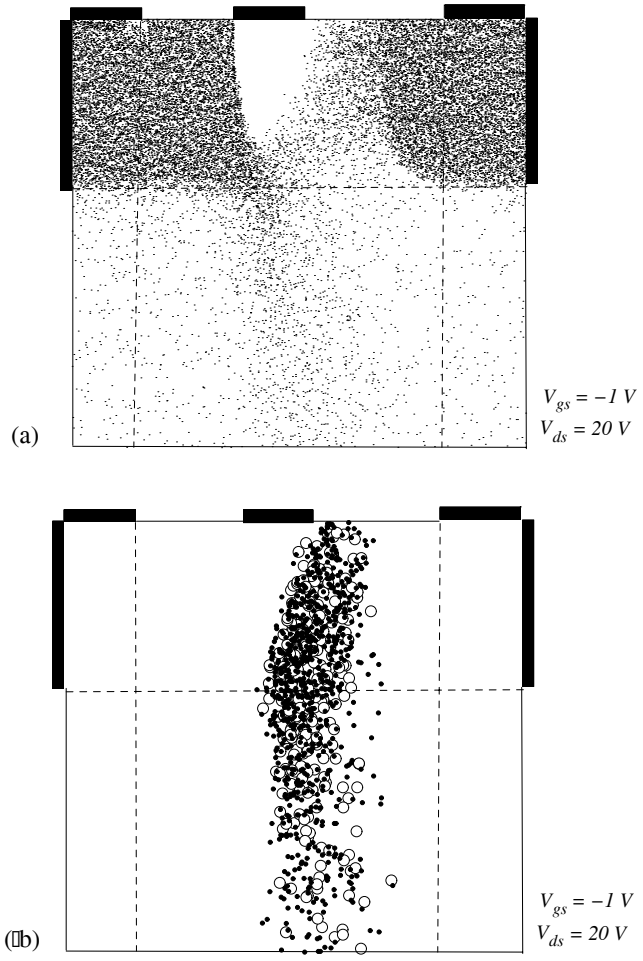

Fig. 3. The distribution of hot electrons at room temperature for $V_{gs} = -1$ V, $V_{ds} = 20$ V in (a) central Γ valley and (b) upper valleys.

displacement, so resembles the derivative of the sinc voltage (V_{gate}). Note that the gate current shown is the sum of the electric displacement, occuring at the left and right hand electrodes. The reproduction of the sinc pulse in the time-dependence of the drain current is easy to discern, despite high frequency noise on the recorded currents, which is a direct consequence of the motion of the finite number of electron particles across the field cell grid in the simulation. The current gain has been derived as a function of frequency by taking fast Fourier transforms of the simulated drain and gate current signals, then obtainning the ratios of the coefficients of the drain and gate current transforms. The calculated cut-off frequency for the simulated device is about 80 ± 5 GHz. If the data are extrapolated to the low frequency limit, the current gain is expected to be of the order of 32 dB.

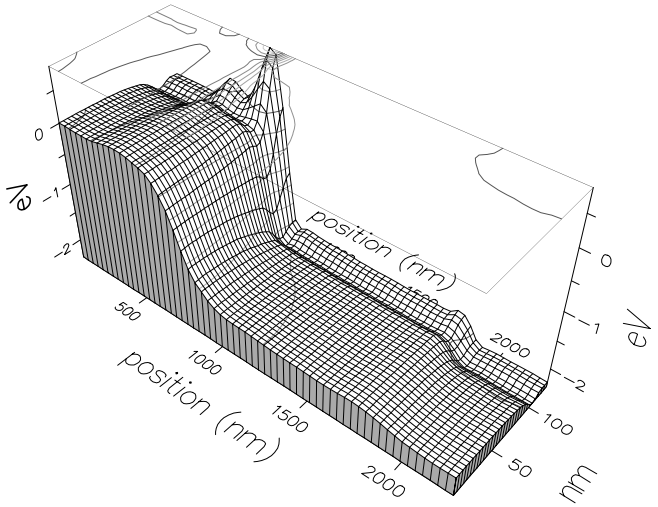

Fig. 4. Interpolated contour plot showing the steady state Γ-valley band profile through the simulated ZnO MESFET at room temperature when the bias applied to the gate is −1 V and the drain-source bias is 20 V.

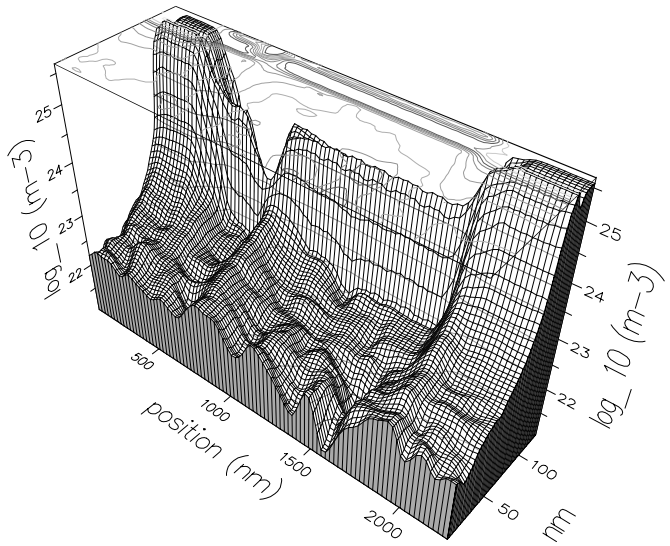

Fig. 5. Logarithmic plot indicating the electron density throughout the modeled region of the ZnO MESFET when the bias applied to the gate is −1 V and the drain-source bias is 20 V.

4. Conclusion

A Monte Carlo simulation was used to model steady-state and transient electron transport in a ZnO metal semiconductor field effect transistor. Our simulation results show that due to the high drain current density, we can expect ZnO devices

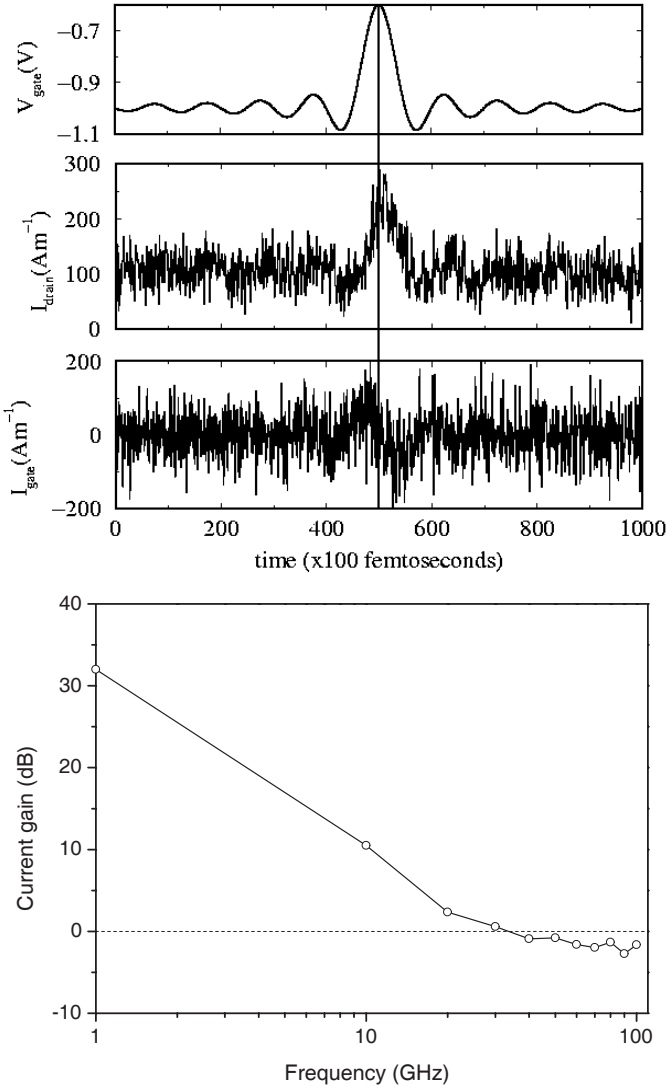

Fig. 6. The simulated frequency response of ZnO MESFET to a sinc gate voltage pulse. From top to bottom, this figure shows the gate voltage (V_{gate}) as a function of time for a truncated pulse of duration 100 ps, the drain current response (I_{drain}) and the gate current (I_{gate}) which is electric displacement. The maximum intrinsic current gain is shown in the logarithmic plot.

have superior high-power and high-gain performance. The frequency response of the device has also been studied by applying a sinc pulse and sinusoidal signals at a range of frequencies to the gate. Due to the high intrinsic cut-off frequency ($\cong 80 \pm 5$ GHz) the present results can also provide the useful advanteges of ZnO MESFET for high frequency performance.

Acknowledgment

This work is benefited from useful discussion with M. G. Paezi.

References

1. D. C. Look, D. C. Reynolds, J. R. Sizelove and W. C. Harsch, *Solid State Commun.* **105** (1998) 399.
2. Y. Chen, D. M. Bagnall, H. J. Koh, K. T. Park, Z. Q. Zhu and T. Yao, *J. Appl. Phys.* **84** (1998) 3912.
3. P. Fons, K. Iwata, S. Niki, A. Yamadaand K. Matsubara, *J. Crystal Growth* **201** (1999) 627.
4. R. D. Vispute, V. Talyansky, Z. Trajanovic, S. Choopun, M. Downes, R. P. Sharma and A. A. Iliadis, *Appl. Phys. Lett.* **70** (1997) 2735.
5. J. Narayan, K. Dovidenko, A. K. Sharma and S. Oktyabrskay, *J. Appl. Phys.* **84** (1998) 2597.
6. Y. Segawa, A. Ohtomo, M. Kawasaki, H. Koinuma, Z. K. Tang, P. Yu and G. K. L. Wong, *Phys. Stat. Sol.* **202** (1997) 669.
7. Y. Liu, C. R. Gorla, S. Liang, N. Emanetoglu and M. Wraback, *J. Electron Mater.* **29** (2000) 69.
8. B. Hahn, G. Heindel and W. Gebhardt, *Semicond. Sci. Tech.* **13** (1998) 788.
9. M. Kasuga and S. Ogawa, *Jpn. J. Appl. Phys.* **22** (1983) 794.
10. N. Takahashi, K. Kaiya and H. Yamamoto, *Jpn. J. Appl. Phys.* **38** (1999) L454.
11. A. Ohtomo, M. Kawasaki, T. Koida and Y. Segawa, *Appl. Phys. Lett.* **72** (1998) 2466.
12. F. M. Hossain, J. Nishii, S. Takagi, A. Ohtomo and T. Fukumura, *Appl. Phys. Lett.* **94** (2003) 7768
13. J. Nishii, F. M. Hossain, T. Aita, Y. Ohmaki, S. Kishimoto and K. Kawasaki, *Jpn. J. Appl. Phys.* **42** (2003) L347.
14. B. J. Chen, X. W. Sun, C. X. Xu and B. K. Tay, *Physica E* **21** (2004) 921.
15. Y. Yoon, J. Lin, S. Pearton and J. Guo, *J. Appl. Phys.* **101** (2007) 24301
16. H. Arabshahi, *Mod. Phys. Lett. B* **20** (2006) 787.
17. H. Arabshahi and M. H. Ghasemian, *Mod. Phys. Lett. B* **22** (2006) 1397.